

Anisotropic and nonlinear metasurface for multiple functions

Zhangjie LUO^{1,2}, Xueyao REN³, Qiang WANG¹, Qiang CHENG^{1,2} & Tiejun CUI^{1,2*}¹State Key Laboratory of Millimeter Waves, School of Information Science and Engineering, Southeast University, Nanjing 210096, China;²Pazhou Lab, Guangzhou 510330, China;³Air and Missile Defense College, Air Force Engineering University, Xi'an 710051, China

Received 16 March 2021/Revised 8 May 2021/Accepted 17 May 2021/Published online 18 August 2021

Abstract We present a novel anisotropic and nonlinear metasurface integrated with multiple functions of diffuse scattering, beam splitting, and normal reflection, which can be switched in real time by tuning the polarization state or power level of the incident microwave. The key lies in the two judiciously designed anisotropic nonlinear particles in subwavelength scales that possess opposite reflection phases under one polarization and the same nonlinear power-dependent reflection phases under the orthogonal polarization. These properties are demonstrated comprehensively via comparisons between their reflection responses, receiving abilities, and nonlinear circuitry behaviors. In addition, both the spatial arrangement and the electrically enabling strategy of the particles are underpinned to pursue the proposed functions, which are verified through numerical simulations and measurements. When the metasurface is illuminated by plane waves coming from the direction perpendicular to it, a significant beam splitting effect is achieved with strong x -polarized incidence, which is switched to a specular reflection when the incoming power decreases. Under y -polarization, a diffuse scattering phenomenon is obtained, which is not dependent on the incident intensity. The study is expected to offer new solutions to many electromagnetic scenarios involving energy transmissions and protections.

Keywords multi-function, metasurface, nonlinear, anisotropic, polarization

Citation Luo Z J, Ren X Y, Wang Q, et al. Anisotropic and nonlinear metasurface for multiple functions. *Sci China Inf Sci*, 2021, 64(9): 192301, <https://doi.org/10.1007/s11432-021-3264-9>

1 Introduction

Along with increasingly complex electromagnetic (EM) environment and rigorous requirements of EM wave manipulations, multi-functional devices are more of interest than those with fixed performances in terms of relatively low cost, compact configuration, and high switching speed, not only in optics [1, 2] but also in the microwave community [3]. Conventionally, performances of a device can be switched manually through mechanical approaches, e.g., by tuning the relative position of the components [4]. It can be also completed by adjusting variables such as light intensity [5], digital signal [6–9], temperature [10], posture of the device [11].

Besides the above methodologies, multi-functional devices were also proposed based on incident EM waves. Compared with features such as frequency [12, 13], intensity [14, 15], direction [16], and spin angular momentum [17], the utilization of polarization state has been proved to be a popular method. Under different incident polarization states, a rich number of multi-functional devices were delicately designed, such as beam splitters [18, 19], chiral structures [20, 21], antenna [22], holographic devices [23, 24]. On the other hand, intensity-dependent multi-functional devices also attract more and more attention since the beginning of this century [25]. Under varying incident intensity, these devices performed differently, thus exhibiting nonlinear properties such as resonance shifting [26, 27], self-adaptive absorption [28–30], nonreciprocity [31–34], and beyond. Different from the nonlinear phenomena in the optical community,

* Corresponding author (email: tjcui@seu.edu.cn)

microwave nonlinearity was traditionally based on the metamaterial structure, i.e., the split-ring resonator (SRR), integrated with nonlinear components like varactor diodes [25]. One may notice that, however, most of the existing nonlinear metamaterials operate under a specific polarization state only, ignoring the orthogonal one. If a nonlinear metamaterial is equipped with the capability of polarization manipulation, its application range can be largely extended. To do this, the structural anisotropy should be engineered delicately so that it can perform differently under orthogonal polarizations. Besides, the spatial arrangement of the nonlinear anisotropic particles should be purposely designed, e.g., a random distribution for the diffusing effect [6], or a phase-gradient distribution for the beam deflection [35]. Unfortunately, since the passive SRR conducts the nonlinearity by combining the intensity-sensing and property-tuning together, a tiny anisotropic adjustment would result in a remarkable deterioration of the nonlinear property under the main polarization. This motivates our strong interest in this work.

In this paper, we break the integration of the nonlinear process of the conventional SRR by adopting an active intensity-dependent sub-wavelength particle. The intensity-sensing and property-tuning stages of the nonlinearity are performed independently by different components, so that they are considered separately, thus with more degrees of freedom to pursue the nonlinearity and anisotropy. The special emphasis of this work is put on the two distinctions that contribute to the novel multi-functional metasurface. Firstly, two anisotropic nonlinear particles, possessing almost the same nonlinear reflection coefficients under x -polarization and opposite reflection phases under y -polarization, are proposed to comprise the metasurface. These characteristics are achieved through comprehensive and deep investigations on their reflection features under orthogonal polarizations, receiving properties, and power-dependent behaviors. Secondly, the judicious strategies of the nonperiodic spatial distribution and direct-current (DC) biasing for the particles are highlighted, giving birth to the metasurface with multiple functions triggered by the incident power or polarization. When x -polarized plane waves impinge on the metasurface from the broadside direction, i.e., perpendicular to the plane, EM energy is reflected normally or split into two symmetric beams, which are switched by altering the incident power level. When the polarization changes to the orthogonal one, the incident energy is diffused into numerous directions, which is not dependent on the power.

The organization of this paper is arranged as follows. Section 2 presents the configurations and properties of the two anisotropic particles. In Section 3, the nonperiodic distributing solution of the particles and their biasing strategy are introduced. After that, the diffuse scattering effect and power-triggered beam manipulations are studied with simulated and experimental results. Finally, a conclusion is drawn in Section 4.

2 The design of anisotropic nonlinear particles

The proposed nonlinear particles exhibit reflection phases varied by the intensity of x -polarized waves. It is an active printed-circuit-board configuration that contains the metallic patches and varactors on the top layer, the metallic reflecting ground on the middle layer, and the radio-frequency (RF) detecting circuit on the bottom, as depicted in the 3D view in Figure 1(a). The metallic layers are separated by two substrates (F4B with a dielectric constant of 2.65 and loss tangent of 0.001). The varactor diode is located between the two patches with the cathode on the larger patch. Two vertical metallic vias connect the top patches and the bottom circuit, without touching the middle layer due to the two-round clearances on it.

In the nonlinear mode, the patches capture the x -polarized wave and transmit a small portion of incoming energy to the circuit through Via 1. The circuit interprets the incident intensity and generates a corresponding DC signal to bias the varactor on the top through Via 2. Because the reflection phase of the particle is determined by the capacitance of the varactor, it is therefore controlled by the wave intensity. When the circuit is deactivated, the reflection phase is constant.

Two particles, called Particles A and B, are designed with different top patches, aiming at having their reflections under y -polarization out of phase, while maintaining the nonlinear reflection behaviors under x -polarization as close as possible. As mentioned before, this is difficult for the particles of conventional nonlinear metamaterials, but can be realized by the proposed configuration. Through a series of optimizations using parameter sweeping, the structural parameters of the particles and circuit components are finally obtained, some of which are listed in Figure 1. The diameter of the vias is 0.8 mm, and that of the clearances on the middle layer is 1.6 mm. As can be found from the top views of the two particles

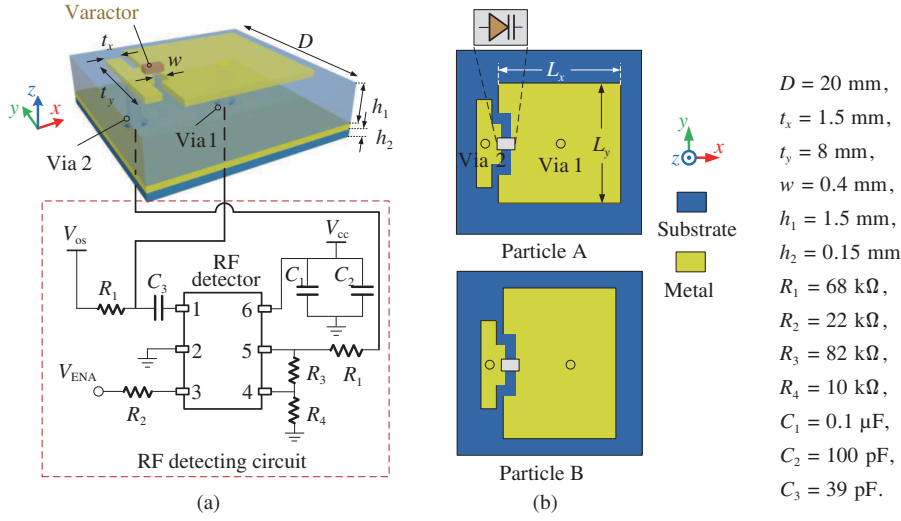


Figure 1 (Color online) (a) 3D view of the particle together with the detecting circuit integrated on the bottom layer; (b) top views of Particles A and B, showing the different sizes of the patches and different positions of Via 1.

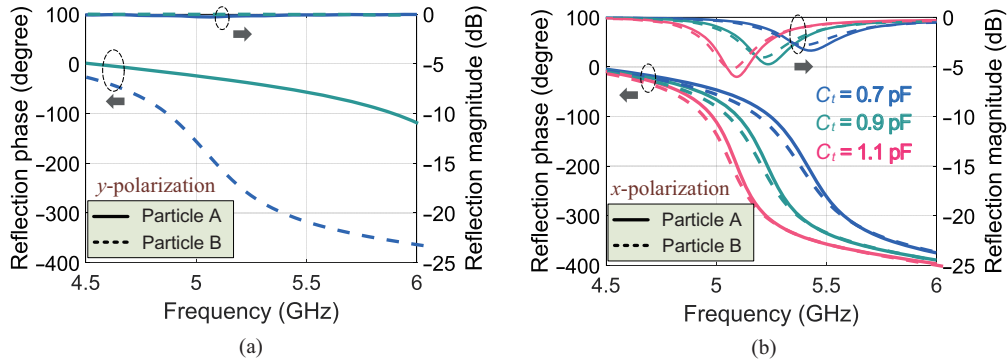


Figure 2 (Color online) (a) Simulated reflection magnitudes and phases of Particles A and B when they are illuminated by y -polarized plane waves. The varactor capacitance is 0.7 pF. Results with 0.9 and 1.1 pF are omitted because they would overlap if placed together. (b) When illuminated by x -polarized plane waves, the reflection magnitudes and phases of the two particles as functions of the capacitance of the varactor C_t .

displayed in Figure 1(b), the dimensions of the larger patches are different. For Particle A, $L_x = L_y = 13$ mm; for Particle B, $L_x = 13$ mm, and $L_y = 16.5$ mm. Also, Via 1 of Particle A is at the center of the patch, while the via of Particle B is moved by 0.7 mm along $+x$ direction. The detecting chip is LTC5530 from Linear Technology.

2.1 Anisotropic reflection coefficients

The reflection features of the particles are retrieved from numerical simulations using the commercial software, CST Microwave Studio 2016. By setting a waveguide port facing the top of the particle and electric (E) and magnetic (M) boundary conditions along the x - and y -directions, the scattering parameters of an infinite lattice of the particles under the plane-wave illuminations from the broadside are calculated. When the E boundaries are placed along the x -direction and the M boundaries are set along the y -direction, the plane wave is x -polarized. By switching the E and M boundaries, the polarization changes to the y -direction. The varactor on the top layer is modeled using a resistor-inductor-capacitor (RLC) series circuit. Skyworks SMV1232 is chosen in this work with the parasitic resistance of 1.5 Ω and inductance of 0.8 nH.

The reflection coefficients of Particles A and B under y -polarization are simulated with various varactor capacitance values. Because the varactor is placed along the other direction, the capacitance has very little impact on the reflection under this polarization. Figure 2(a) gives the reflection magnitudes and phases of the two particles with the capacitance of 0.7 pF. The results with other values, i.e., 0.9 pF, 1.1 pF, are omitted here since they overlap with each other and cannot be distinguished. Observing

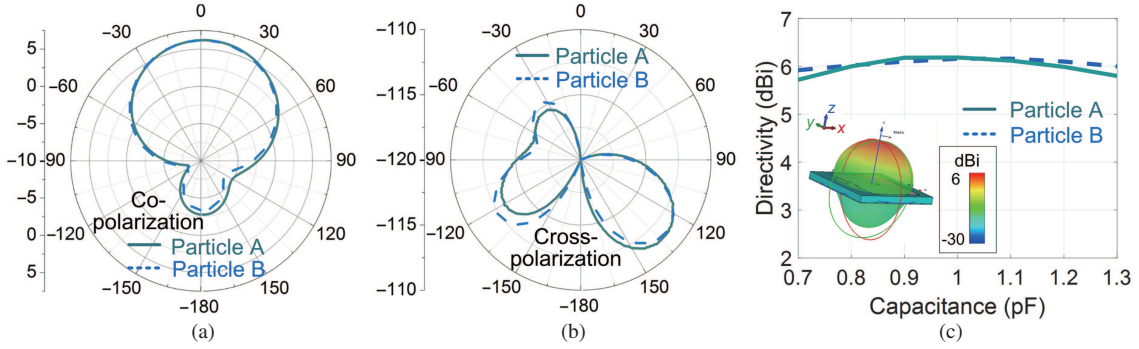


Figure 3 (Color online) Simulated radiation performances of a single Particle A and a single Particle B at 5.2 GHz. (a) Far-field co-polarized patterns; (b) far-field cross-polarized patterns; (c) the impact of the capacitance of the varactor on the directivities of the particles. A 3D pattern is given in the inset.

the figure, it is found that in the frequency region from 5.05 to 5.20 GHz, the phase difference between them varies from 150° to 210° , which is a promising range for the diffusing effect if they are arranged purposely [6]. The magnitude of the reflection remains high in the frequency band, indicating a low loss under this polarization.

The reflection coefficients under x -polarized illumination are shown in Figure 2(b). While the capacitance of the varactor is increasing, the resonances of the particles move from higher frequencies to lower ones. For this reason, the reflection phase changes at the frequencies of our interest. The simulated results show that when the capacitance varies from 0.7 to 1.1 pF, the phase changes in a range of about 180° at around 5.2 GHz, which is enough for the beam splitting effect. Due to the parasitic resistance of the varactor, the reflection magnitudes are larger than -4.5 dB. We remark that, although the two particles offer a large phase difference under y -polarization, their phase changes under x -polarization are very close to each other, as clearly shown in Figure 2(b).

2.2 Radiation characteristics under x -polarization

In the last session, it is apparent that the top patches scatter with the capacitance-tuned phase under the x -polarized illumination. Besides, they also behave as receiving components that couple a small portion of EM energy into the circuit through Via 1. According to the time-reversal symmetry, or reciprocity, the radiating and receiving performances of a normal device should be identical. Therefore, to examine the wave-reception capability of the particles, their radiating directivities pointing to the normal direction and input characteristics, which are described by the reflection coefficients at the interface between Via 1 and the circuit, are studied.

To begin with, the radiation performances of a single particle are analyzed using full-wave simulations. To feed the radiator during the simulation, a wave port is set on the bottom layer at the end of a very short microstrip (with a width of 1.5 mm and a length of about 1 mm), with the other end connected to Via 1. The far-field performances of a single Particle A and a single Particle B at 5.2 GHz are compared in Figure 3. The co-polarized and cross-polarized patterns with $C_t=1$ pF are shown in Figures 3(a) and (b), respectively, implying the main beams pointing the broadside direction and good polarization purity of the particles. The direction of the main lobes is not affected by the variation of the varactor capacitance, but the directivities at the broadside experience tiny variations due to a small impact of the capacitance on the back lobe. Figure 3(c) displays the directivities in the normal direction at 5.2 GHz as functions of the capacitance. Values larger than 5.7 dBi are achieved with the capacitance ranging from 0.7 to 1.3 pF.

In order to transmit enough energy into the circuit, the input impedance of the particle, or called radiator, at the interface between Via 1 and the circuit at the bottom layer should, in an ideal case, match the input impedance of the RF_{in} pin (Pin 1) of the detector, which is about 20 Ω according to the datasheet of the detector. If the radiator is regarded as a half-wave rectangular patch antenna fed by a coaxial line, its input impedance can be theoretically predicted by [36]

$$Z_{\text{in}} = 90 \frac{\epsilon_r^2}{\epsilon_r - 1} \left(\frac{L_x}{L_y} \right)^2 \cos^2(\pi \Delta x / L_x) \Omega, \quad (1)$$

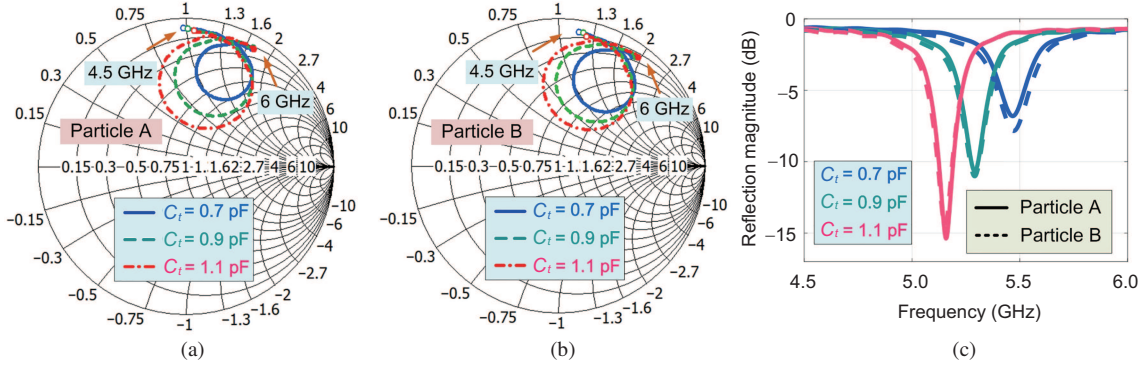


Figure 4 (Color online) Simulations on the input impedance of Particles A and B as radiators on the interfaces between Via 1 and the bottom circuits, referring to the input impedance of the circuit, as functions of the varactor capacitance. (a) Input impedance of Particle A. (b) Input impedance of Particle B. (c) Reflection magnitudes of the two particles.

where ϵ_r is the relative dielectric constant of the substrate; L_x and L_y are the dimensions of the larger patch of the particle along x - and y -directions, respectively; Δx is the distance between the right edge of the patch and Via 1. Based on the structural parameters, the real parts of the input impedance of the radiators are between 0 and 20Ω at 5.2 GHz, yet with an inductance introduced by the via. It should be mentioned that the above theoretical equation is suitable for a standard microstrip antenna with a rectangular patch. It does not consider the bending edge of the patch in this work and the varactor capacitance, which affect the effective resonant length of the radiator and hence its input impedance around 5.2 GHz.

To have a more accurate investigation of the input impedance characteristics, full-wave simulations are conducted. Figures 4(a) and (b) show the input impedances of the two particles versus frequency in the Smith Chart considering the input impedance of the circuit chip. It is clear that the input impedances are strongly affected by the capacitance. Based on the impedance values, magnitudes of reflection coefficients, or $|S_{11}|$, at the interface as functions of the capacitance are obtained in Figure 4(c). Although the impedances of the radiators do not exactly match that of the chip in the whole frequency band, the $|S_{11}|$ dips still allow some energy to enter the circuit at around 5.2 GHz. It can be observed that, when the capacitance increases, the reflection magnitudes at 5.2 GHz decrease, which means the proportion of EM energy injected into the circuit increases. As will be discussed later, when the incident power increases, the reversely biasing voltage across the varactor decreases, which means the increase of the capacitance. In other words, the stronger the incident power is, the larger proportion of the EM energy goes into the circuit, which further enhances the nonlinear behaviors.

2.3 Performances of the detecting circuits

As illustrated in Figure 1, the RF detecting circuit is distributed on the bottom layer of each particle. Pin 1 of the detector is connected to Via 1 through C_3 . The DC output is generated by Pin 5, which is connected to Via 2 through R_1 . The circuits and their layouts for Particles A and B are strictly the same.

When Pin 3 is applied with a high voltage level, the circuit is enabled. In addition to V_{cc} for supplying the detector chip, an offset voltage, namely V_{os} , is connected to Via 1 through R_1 . V_{os} is set to be always larger than the output voltage of the detector for the following two reasons. Firstly, the varactor is reversely biased all the time, and the reverse voltage decreases with the increasing incoming power. As a result, the capacitance of the varactor is enhanced by the power. Secondly, the operating voltage point of the varactor can be altered flexibly by changing the offset voltage, thus adding one more degree of freedom in adjusting the capacitance range. An output buffer amplifier is integrated inside the detector chip, and the gain of the amplifier can be set by R_3 and R_4 using

$$\text{Gain} = 1 + R_3/R_4. \quad (2)$$

By adjusting these two components, the maximum DC output of the circuit can be set.

To evaluate the performances of the circuit together with the particles, two samples of Particles A and B are fabricated with the varactors and circuits respectively loaded on the top and bottom. The particle

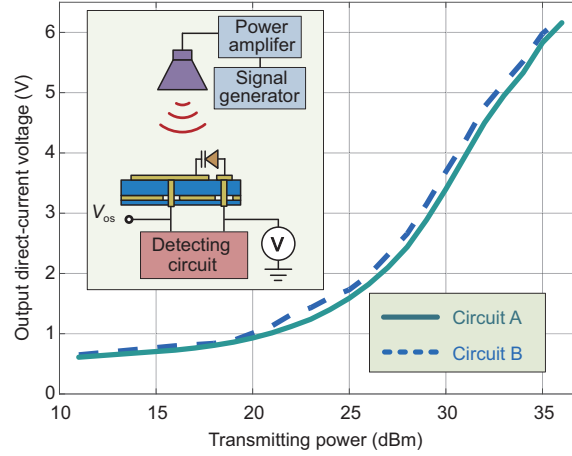


Figure 5 (Color online) Measured DC output voltages of the detecting circuits of Particles A and B when they are illuminated by the x -polarized microwaves with varying power levels. The measurement setup is plotted in the inset, not to scale.

Table 1 Reflection phase responses of the particles

Incident polarization	V_{ENA}	Particle A or B
y -polarization	NA	Reflection phases of A and B are opposite ^{a)}
x -polarization	High	Both particles show synchronously power-dependent reflection phase (nonlinear mode)
x -polarization	Low	Both particles show the same constant reflection phase, not affected by incident power (linear mode)

a) This property has nothing to do with the microwave power or V_{ENA} .

sample is placed 1 m away from the aperture of a standard rectangular horn antenna with a gain of 15 dBi from 3.9 to 5.9 GHz. Microwave signals are generated by a signal generator, amplified by a power amplifier (PA), and transmitted by the horn, as sketched in the inset of Figure 5. The offset voltage V_{os} is set to be 11 V.

The voltages at the anode of the varactors are monitored by a voltage meter and recorded in Figure 5. It is easily observed that the circuits of Particles A and B provide almost the same DC voltages, which is expected considering their similar radiation performances and the same circuit design. When the incoming power changes from 11 to 36 dBm, the DC voltages range from about 0.7 to 6.1 V. This indicates that the reverse voltage across the varactor changes from 10.3 to 4.9 V. According to the performance of the chosen varactor, the capacitance range is between 0.75 to 1.05 pF with this voltage range. Referring to the aforementioned x -polarized reflection phase that is related to the varactor capacitance, it is reasonable to deduce that the phase can be tuned in a range of 180° by altering the incident power, and, more importantly, these nonlinear behaviors are achieved synchronously by Particles A and B. On the other hand, if the circuit is deactivated by a low level applied to Pin 3, the voltage across the varactor is 11 V, and the capacitance is about 0.75 pF, disregarding the incident power. In this case, the particles degenerate back into linear ones with the constant reflection phases.

3 Scattering performance of the metasurface

Table 1 is established to summarize the properties of Particles A and B, under y - or x -polarized broadside illuminations and different enabling voltages for the particle circuits. Under y -polarization, the two particles show opposite reflection phases within the frequency region of our interest, and this is not changed by the microwave power or the circuit, so they are considered to be different particles. On the other hand, under x -polarization, they exhibit almost the same properties. When a high enabling voltage is applied to the circuit, they operate in the nonlinear mode, offering power-dependent reflection phases; when the voltage becomes low to disable the circuit, they are in the linear mode with the constant phase and not impacted by the incident power.

A metasurface is constructed by delicately distributing a number of Particles A and B on a panel. Theoretically, the particles can be distributed at will on the surface and controlled by enabling voltages individually, and the scattering performances of the metasurface are determined by their phase distribution. If opposite phases are arranged periodically on the surface along the y -direction, according to the

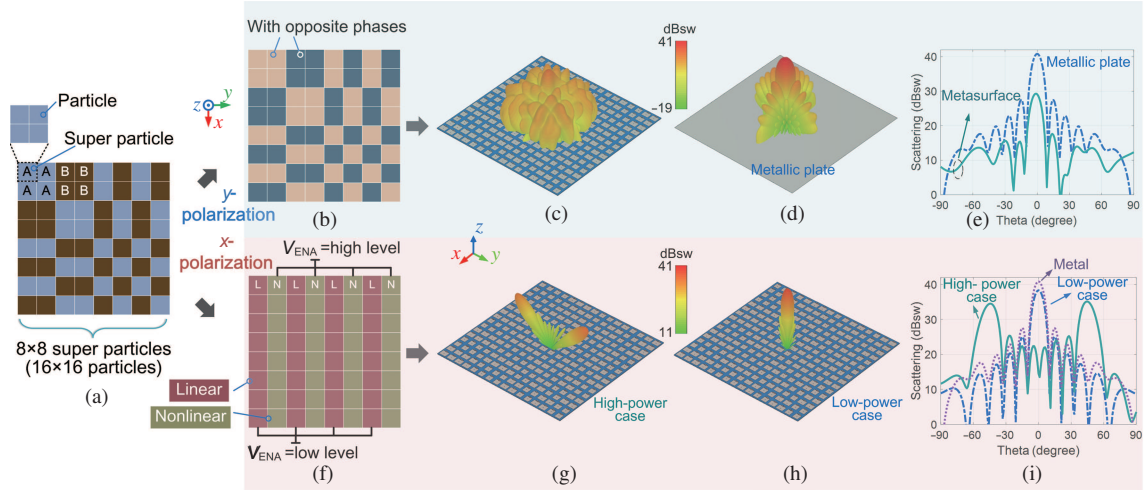


Figure 6 (Color online) (a) Spatial arrangement of the particles on metasurface. (b) Under y -polarization, the reflection phases of Particles A and B are opposite. The figure shows the distribution of the opposite-phase super particles. (c) Simulated scattering far-field 3D pattern of the metasurface under y -polarization at 5.2 GHz. The “sw” in the color bar stands for “square wavelength”. (d) Simulated scattering far-field 3D pattern of the same-sized metallic plate at 5.2 GHz. (e) Comparison of the scattering at 5.2 GHz between the metasurface and the metallic plate, obtained from simulations. (f) Under x -polarization, Particles A and B are considered as the same particle. 8 columns of the super particles are alternatively applied with high and low enabling voltage levels, making the columns exhibiting nonlinear or linear reflection phase responses, respectively. (g) Simulated 3D far-field pattern at 5.2 GHz with high-power x -polarized excitation. (h) Simulated 3D pattern at 5.2 GHz with low-power x -polarized excitation. (i) Simulated 2D scattering patterns at 5.2 GHz of the metallic plate and the metasurface in the high-power and low-power cases.

generalized Snell’s law [35], incoming EM energy will be deflected into two symmetric directions on the yo -plane, and the elevation angles of the split beams can be theoretically calculated by [6]

$$\theta = \arcsin(\lambda/\Gamma_y), \quad (3)$$

where λ is the wavelength in free space, and Γ_y is the period of the phase change along the y -direction. It is clear that Γ_y should be larger than λ , otherwise the incoming energy would be converted into surface waves, rather than being deflected [37]. Considering that the size of a single particle is 20 mm, and the operating wavelength is about 57.7 mm (corresponding to 5.2 GHz), the smallest number of the particle with the same phase should be two such that the phase period can be larger than the wavelength.

As an illustrating example, we choose 2×2 particles as the smallest group, which is called a super particle, as plotted in Figure 6(a). The metasurface is composed of 8×8 super particles (totally 16×16 particles). The super particles are arranged along x - and y -directions with the sequences “AABBABAB”, respectively. In this case, the metasurface under y -polarization exhibits the purposely-designed phase distribution, as shown in Figure 6(b), which accounts for the diffusing effect. In addition, the 8 columns of the super particles, no matter A or B, are alternatively applied with high and low enabling voltages for their circuits, thus realizing the alternative nonlinear and linear phase distributions along y -direction when x -polarized waves impinge on the metasurface, as illustrated in Figure 6(f). When the power of x -polarized waves changes, the reflection phases of the linear particles remain constant, and those of the nonlinear particles vary accordingly, leading to the power-triggered beam controlling effect.

3.1 Numerical simulations

The scattering performances of the metasurface are simulated using CST. Under y -polarization, the simulated 3D scattering pattern at 5.2 GHz is presented in Figure 6(c). It is clear that the energy is redirected into various directions by the metasurface, and the backscattering is obviously suppressed. As a comparison, the dominant reflection of a same-sized metallic plate under the illumination is presented in Figure 6(d). A more detailed comparison of the pattern on the yo -plane is made in Figure 6(e), from which a backscattering reduction of more than 10 dB can be observed.

For x -polarization simulations, the varactors are also modeled using the series RLC circuit. The capacitance for the linear particles is fixed to be 0.75 pF. The capacitances for the nonlinear particles in the high- and low-power cases are set to be 1.05 and 0.75 pF, respectively. Figures 6(g) and (h) present the simulated scattering far-field patterns of the metasurface at 5.2 GHz in the strong and weak incidence

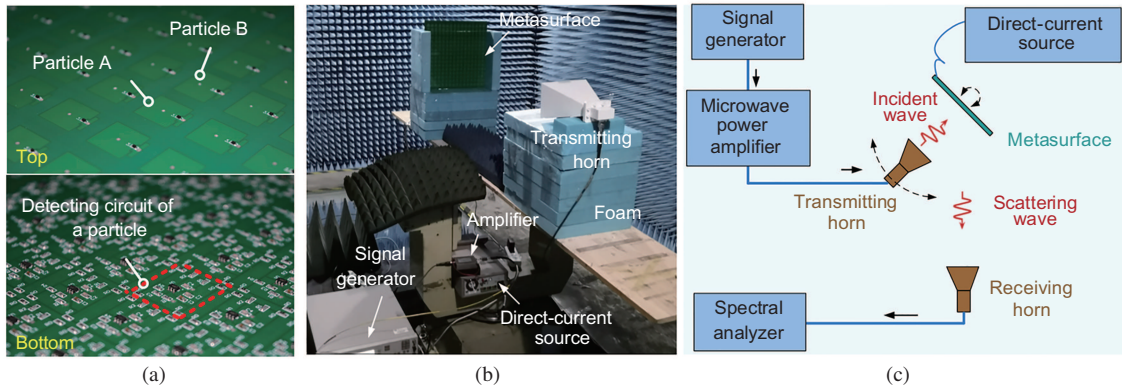


Figure 7 (Color online) (a) Photographs of the metasurface prototype; (b) photograph of the measurement setup, without the receiving antenna and the spectral analyzer; (c) schematic of the measurement system, not to scale.

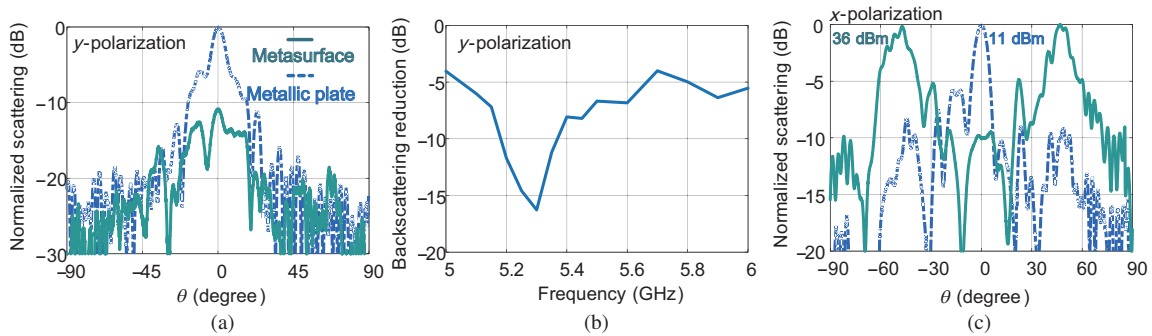


Figure 8 (Color online) (a) Measured scattering comparison between the metasurface and the same-sized metallic plate at 5.2 GHz, under y -polarization. (b) Measured backscattering reduction of the metasurface over the frequency region of our interest, under y -polarization. (c) Measured normalized 2D scattering patterns when the metasurface is excited by x -polarized microwaves, showing the beam splitting effect with 36-dBm power and specular reflection phenomenon with 11-dBm power.

cases, respectively. It is clear that two symmetrically split beams are generated with high power, owing to almost opposite phases between the nonlinear and linear particles. The elevation angle is about 46° , which agrees well with the prediction from (3), corresponding to the split angle of about 92° . In the low-power case, the phase difference between the nonlinear and linear particles is zero, so a normal reflection is obtained by the metasurface. Together with the 2D patterns on the yo -plane compared in Figure 6(i), it is shown that the beam-splitting and reflection performances of the metasurface can be easily switched by tuning the power of microwaves. In addition, the 2D scattering pattern of the metallic plate is also plot in Figure 6(i), from which a slightly higher value at $\theta = 0^\circ$ is observed compared with the low-power case of the metasurface. The loss of metasurface is attributed to the lossy substrate and varactor resistance.

3.2 Measurements

A metasurface prototype is fabricated using the standard printed-circuit-board and surface-mount technologies, and pictures of the top and bottom layers are presented in Figure 7(a). Far-field measurements are carried out in a standard microwave chamber. The metasurface under test and the transmitting horn, which is used before for the circuit test, are placed on a supporting board with a distance of 1 m. The board rotates with a mechanical turntable from -90° to 90° . The transmitting horn is connected with an RF PA, which amplifies the microwaves generated by a signal generator (Agilent E8257D). The energy scattered by the prototype is received by a wide-band receiving horn antenna and finally fed to a spectral analyzer (Agilent E4447A), which are placed more than 6 m away. $V_{os} = 11$ V, $V_{cc} = 6.5$ V, and enabling voltages V_{ENA} for the nonlinear particles are provided by a DC power source (ITECH IT6332A). The experiment setup is sketched in Figure 7(c), and a photograph is given in Figure 7(b), including the metasurface prototype, transmitting horn, amplifier, signal generator, foams, and DC source.

The experiment starts with a y -polarized incidence. Figure 8(a) gives the normalized scattering far-field patterns of the metasurface and a metallic plate with the same size, indicating a backscattering reduction of 11.7 dB at 5.2 GHz. The backscattering of the metasurface and the metallic plate over

the frequency range from 5.0 to 6.0 GHz is also measured. The result in Figure 8(b) indicates that the reduction is larger than 7 dB from 5.15 to 5.45 GHz, and the largest one occurs at 5.3 GHz with a value of 16.3 dB.

By rotating the transmitting horn by 90° , measurements under x -polarization are conducted. The scattering far-field patterns on the H-plane are measured with the incident power levels of 11 and 36 dBm, and the normalized results are given in Figure 8(c). When the power is low, a single beam is observed in the direction of $\theta = 0^\circ$, which means that the microwave is reflected specularly by the metasurface. In contrast, the beam is symmetrically split into two when the power is 36 dBm, and the magnitude in the normal direction is lower than the beam peaks occurring at $\theta = \pm 47^\circ$ by about 10 dB. These results agree quite well with the simulations shown in Figures 6(e) and (i), serving as solid validations for our design.

4 Conclusion

In summary, a multifunctional metasurface consisting of two types of anisotropic nonlinear particles is proposed. The functionalities of the metasurface include diffuse scattering, beam splitting, and normal reflection. By changing the polarization or power level of incident waves, these functions can be promptly switched at will. The configurations of the particles, their anisotropic reflection phases, receiving properties, and circuit behaviors are elaborated in this paper, proving that they exhibit opposite reflection phases under y -polarization and almost identical nonlinear phases under x -polarization. On the proposed metasurface, these particles are purposely arranged with a specific sequence and delicately biased by enabling strategies. Numerical simulations and experimental measurements are performed to verify the functionalities of the metasurface. The results show that, under y -polarization, backscattering reductions of more than 10 dB are achieved at the frequencies of our interest, which is not affected by the incident power. With strong x -polarized excitation of 36 dBm, the beam splitting phenomena is clearly observed with the dip of 10 dB between the peaks. By applying a low incident power of 11 dBm, a single reflected beam is obtained immediately. Equipped with the flexibly controllable functionalities together with the advantages of low profile and easy fabrication, this nonlinear metasurface can potentially find a variety of applications such as EM energy transferring, power redistributing, and nonlinear power protection.

Acknowledgements This work was supported by National Natural Science Foundation of China (Grant No. 61801117), Fundamental Research Funds for the Central Universities (Grant No. 2242021R10109), National Key Research and Development Program of China (Grant Nos. 2017YFA0700201, 2017YFA0700202, 2017YFA0700203), International Cooperation and Exchange of National Natural Science Foundation of China (Grant No. 61761136007), the 111 Project (Grant No. 111-2-05), and Zhishan Young Scholar Program and Zijin Scholar Program of Southeast University.

References

- 1 Chen S, Liu W, Li Z, et al. Metasurface-empowered optical multiplexing and multifunction. *Adv Mater*, 2020, 32: 1805912
- 2 Zhang F, Xie X, Pu M, et al. Multistate switching of photonic angular momentum coupling in phase-change metadevices. *Adv Mater*, 2020, 32: 1908194
- 3 Zhang Y, Liu H, Cheng H, et al. Multidimensional manipulation of wave fields based on artificial microstructures. *Opto-Electron Adv*, 2020, 3: 200002
- 4 Sievenpiper D, Schaffner J, Loo R, et al. A tunable impedance surface performing as a reconfigurable beam steering reflector. *IEEE Trans Antenn Propagat*, 2002, 50: 384–390
- 5 Shadrivov I V, Kapitanova P V, Maslovski S I, et al. Metamaterials controlled with light. *Phys Rev Lett*, 2012, 109: 083902
- 6 Cui T J, Qi M Q, Wan X, et al. Coding metamaterials, digital metamaterials and programmable metamaterials. *Light Sci Appl*, 2014, 3: e218
- 7 Luo Z, Chen M Z, Wang Z X, et al. Digital nonlinear metasurface with customizable nonreciprocity. *Adv Funct Mater*, 2019, 29: 1906635
- 8 Zhang L P, Zhang H C, Tang M, et al. Integrated multi-scheme digital modulations of spoof surface plasmon polaritons. *Sci China Inf Sci*, 2020, 63: 202302
- 9 Wang Q, Jiang W X, Shen H Y. Design of low-profile array antenna working at 110 GHz based on digital coding characterization. *Sci China Inf Sci*, doi: 10.1007/s11432-020-3165-8
- 10 Zhang Y, Wu P, Zhou Z, et al. Study on temperature adjustable terahertz metamaterial absorber based on vanadium dioxide. *IEEE Access*, 2020, 8: 85154–85161
- 11 Ma Q, Bai G D, Jing H B, et al. Smart metasurface with self-adaptively reprogrammable functions. *Light Sci Appl*, 2019, 8: 98
- 12 Wu H T, Wang D, Fu X, et al. Space-frequency-domain gradient metamaterials. *Adv Opt Mater*, 2018, 6: 1801086
- 13 Zhou L, Shen Z. Hybrid frequency-selective rasorber with low-frequency diffusion and high-frequency absorption. *IEEE Trans Antenn Propagat*, 2021, 69: 1469–1476
- 14 Luo Z, Chen X, Long J, et al. Nonlinear power-dependent impedance surface. *IEEE Trans Antenn Propagat*, 2015, 63: 1736–1745
- 15 Li A, Singh S, Sievenpiper D. Metasurfaces and their applications. *Nanophotonics*, 2018, 7: 989–1011
- 16 Chen K, Ding G, Hu G, et al. Directional Janus metasurface. *Adv Mater*, 2020, 32: 1906352

- 17 Li G, Sartorello G, Chen S, et al. Spin and geometric phase control four-wave mixing from metasurfaces. *Laser Photon Rev*, 2018, 12: 1800034
- 18 Ma H F, Wang G Z, Jiang W X, et al. Independent control of differently-polarized waves using anisotropic gradient-index metamaterials. *Sci Rep*, 2015, 4: 6337
- 19 Lee W S L, Nirantar S, Headland D, et al. Broadband Terahertz circular-polarization beam splitter. *Adv Opt Mater*, 2018, 6: 1700852
- 20 Chen M L N, Jiang L J, Sha W E I, et al. Polarization control by using anisotropic 3-D chiral structures. *IEEE Trans Antenn Propagat*, 2016, 64: 4687–4694
- 21 Shadrivov I V, Fedotov V A, Powell D A, et al. Electromagnetic wave analogue of an electronic diode. *New J Phys*, 2011, 13: 033025
- 22 Chen Q, Li J Y, Yang G, et al. A polarization-reconfigurable high-gain microstrip antenna. *IEEE Trans Antenn Propagat*, 2019, 67: 3461–3466
- 23 Li M, Tang M-C, Xiao S. Design of a LP, RHCP and LHCP polarization-reconfigurable holographic antenna. *IEEE Access*, 2019, 7: 82776–82784
- 24 Zhang C, Deng L, Zhu J F, et al. A right-handed circularly polarized wave generated by a waveguide-fed holographic metasurface. *J Phys D-Appl Phys*, 2020, 53: 26LT01
- 25 Pendry J B, Holden A J, Robbins D J, et al. Magnetism from conductors and enhanced nonlinear phenomena. *IEEE Trans Microwave Theor Techn*, 1999, 47: 2075–2084
- 26 Wang B N, Zhou J F, Koschny T, et al. Nonlinear properties of split-ring resonators. *Opt Express*, 2008, 16: 16058–16063
- 27 Slobozhanyuk A P, Lapine M, Powell D A, et al. Flexible helices for nonlinear metamaterials. *Adv Mater*, 2013, 25: 3409–3412
- 28 Sievenpiper D F. Nonlinear grounded metasurfaces for suppression of high-power pulsed RF currents. *Antenn Wirel Propag Lett*, 2011, 10: 1516–1519
- 29 Luo Z, Long J, Chen X, et al. Electrically tunable metasurface absorber based on dissipating behavior of embedded varactors. *Appl Phys Lett*, 2016, 109: 071107
- 30 Li A, Luo Z, Wakatsuchi H, et al. Nonlinear, active, and tunable metasurfaces for advanced electromagnetics applications. *IEEE Access*, 2017, 5: 27439–27452
- 31 Caloz C, Alú A, Tretyakov S, et al. Electromagnetic nonreciprocity. *Phys Rev Appl*, 2018, 10: 047001
- 32 Fernandes D E, Silveirinha M G. Asymmetric transmission and isolation in nonlinear devices: why they are different. *Antenn Wirel Propag Lett*, 2018, 17: 1953–1957
- 33 Sounas D L, Alú A. Fundamental bounds on the operation of Fano nonlinear isolators. *Phys Rev B*, 2018, 97: 115431
- 34 Shi Y, Yu Z, Fan S. Limitations of nonlinear optical isolators due to dynamic reciprocity. *Nat Photon*, 2015, 9: 388–392
- 35 Yu N F, Genevet P, Kats M A, et al. Light propagation with phase discontinuities: generalized laws of reflection and refraction. *Science*, 2011, 334: 333–337
- 36 Stutzman W L, Thiele G A. *Antenna Theory and Design*. 3rd ed. Hoboken: John Wiley & Sons, Inc., 2012. 468–474
- 37 Sun S, He Q, Xiao S, et al. Gradient-index meta-surfaces as a bridge linking propagating waves and surface waves. *Nat Mater*, 2012, 11: 426–431